Quaternary International 497 (2018) 170–177

Contents lists available at ScienceDirect

Quaternary International

journal homepage: www.elsevier.com/locate/quaint

Optical dating of K-feldspar grains from Middle Pleistocene lacustrine sediment at Marathousa 1 (Greece)

Zenobia Jacobs[a,*,1], Bo Li[a,1], Panagiotis Karkanas[b,1], Vangelis Tourloukis[c], Nick Thompson[c], Eleni Panagopoulou[d], Katerina Harvati[c]

[a] ARC Centre of Excellence for Australian Biodiversity and Heritage & Centre for Archaeological Science, School of Earth and Environmental Sciences, University of Wollongong, New South Wales, 2522, Australia
[b] Malcolm H. Wiener Laboratory for Archaeological Science, American School of Classical Studies, Souidias 54, 10676, Athens, Greece
[c] Paleoanthropology, Senckenberg Center for Human Evolution and Paleoenvironment, Eberhard Karls Universität Tübingen, Rümelinstraße 23, 72070, Tübingen, Germany
[d] Ephoreia of Palaeoanthropology-Speleology, Ardittou 34b, 11636, Athens, Greece

A B S T R A C T

Post-infrared infrared stimulated luminescence (pIRIR) measurements are reported for multiple aliquots of potassium-rich feldspar grains from sedimentary deposits at Marathousa 1 and Choremi Mine in the Megalopolis Basin in southern Greece. Ages were obtained for 9 samples from the deposits that over- and underlie as well as include the archaeological and palaeontological deposits at Marathousa 1. These sediments are sandwiched between lignite seams II and III and thought to represent sediment deposition during a single glacial period. A single age was obtained for a sample from Choremi mine. The equivalent dose estimates are based on a newly developed method presented elsewhere, and environmental dose rate determinations followed standard procedures. A specific focus of this paper is the determination of a representative estimate of time-averaged palaeo-water content of the organic and sand-rich deposits and the impact of porosity and compaction on these estimates. Ages are presented using two water content scenarios. These final ages have relatively large uncertainties, making it difficult to accurately assign deposition to a single oxygen isotope stage (OIS). Taking uncertainty into account, sediment deposition at Marathousa 1 occur sometime during OIS 12 and 11 and at Choremi mine during MIS 8. When combined with other proxy information, these results support the interpretation that the peat deposits (represented by lignite seams II and III) were deposited during warm interglacial periods, and that the intervening clastic materials were deposited during glacial periods. In this case, the ages are best interpreted as supporting deposition of sediments during MIS12. This is consistent with one of the proposed age models, but younger than the other.

1. Introduction

Marathousa 1 is a recently discovered Middle Pleistocene site located in the lacustrine sediments of the lignite mines of the Megalopolis basin in southern Greece (Panagopoulou et al., 2015; Harvati, 2016; Tourloukis and Harvati, 2018; Panagopoulou et al., this issue). The site is currently the earliest known stratified archaeological site in Greece and contains a rich lithic assemblage, bone remains of an almost complete elephant, and several other faunal remains. Several cut marks on the elephant remains and other bone suggests that the site represents an elephant butchering site (Konidaris et al., this issue).

Obtaining reliable age estimates for this site using luminescence dating techniques posed some challenges. First, an initial attempt to obtain an age for a single sediment sample, using both quartz optically stimulated luminescence (OSL) and potassium-rich (K) feldspar infrared stimulated luminescence (IRSL) methods was unsuccessful; both the OSL and post-infrared IRSL (pIRIR) signals were in dose saturation and only minimum ages could be calculated. Obtaining a reliable estimate of the equivalent dose (D_e) from K-feldspar grains required the development of a new procedure based on a multiple aliquot regenerative dose (MAR) procedure and the pIRIR signal from K-feldspar grains. This method is presented in Li et al. (2017) and forms the basis for D_e determination in this study. Second, accurate estimation of the average palaeo-water content over the entire burial period from lake sediments are difficult to estimate accurately (c.f. Sugisaki et al., 2012). An accurate estimate of the water content is essential as water attenuates

* Corresponding author.
E-mail address: zenobia@uow.edu.au (Z. Jacobs).
[1] These authors contributed equally to this study.

https://doi.org/10.1016/j.quaint.2018.06.029
Received 19 February 2018; Received in revised form 19 June 2018; Accepted 20 June 2018
Available online 21 June 2018

external radiation and, therefore, lowers the dose rate received by sedimentary grains in its burial environment. A 10% increase in water content, will typically give rise to a ~5% increase in age obtained from K-feldspar grains (e.g., Zander and Hilgers, 2013). Key factors that change the water content over the burial history of lake sediments include compaction and dewatering. Also, significant water loss can happen between field sampling and sample preparation, particularly when water saturated sand samples are encountered.

In this paper, we will present multiple aliquot regenerative dose predose multiple elevated temperature post infrared-infrared (MAR-pMET-pIRIR) age estimates for K-feldspar grains for sediment samples collected from two sites — Marathousa I and Choremi mine — and will pay special attention to the calculation of water content for the lake sediments using a range of different equations to test the sensitivity of the age estimates to our assumptions about palaeo-water content.

2. Site information and age models

The intermountain Megalopolis basin is a post-orogenic graben with a pre-Pliocene basement consisting of Jurassic to Eocene marine sedimentary rocks (flysch, limestone, dolomite and chert), ultramafic Mesozoic rocks, and Palaeozoic to Triassic cystralline rocks (chist, marble and phyllite) (Vinken, 1965). Carbonate rocks dominate the margins of the basin as well as part of the basal floor of the Plio-Quaternary sequence. These rocks produce a very active karstic aquifer which has played a significant role in the formation of the overlying Plio-Quaternary deposits.

The Megalopolis basin comprises more than 250 m of fluvio-lacustrine Pliocene and Pleistocene deposits. The Pleistocene lignite-bearing Marathousa Member is ~200 m thick in the middle of the basin and is overlain by ~30 m of fluvial deposits of the Megalopolis Member (Vinken, 1965). The sedimentary sequence of the site of Marathousa 1, located in the Marathousa Member, comprises bedded sands and silts, organic-rich laminated and massive sandy silts, and intraclast-rich mudflows deposited in the marshy margins of a shallow lake with fluctuating water levels (Fig. 1; Karkanas et al., this issue). The site comprises two excavated areas, A and B, which are 60 m apart. Although the stratigraphy between the excavated areas shows some differences, field stratigraphic observations, and sedimentary, geochemical and microstratigraphic analyses allowed secure correlations of strata between the two areas (Fig. 1; Karkanas et al., this issue). In particular, a lower part of the sequences has been identified in both areas (UB6-UB9 and UA4-UA6: Fig. 1) that comprise subaqueous deposited sediment of generally low organic and carbonate content. Bluish muds with characteristic load deformation features (UB6 and UA4) closes the lower sequence. The upper part of the sequence (UB5-UB2 and UA3-UA2) follows a major hiatus attributed to exposure and erosion. Macroscopic and microscopic sedimentary facies analysis enabled the identification of microstratigraphic episodes of subaerial exposure, reworking, and erosion at this contact. The upper sequence consist of subaqueously emplaced cycles of organic- and carbonate-rich sediment that have been generated by subaerial floods. Further correlation of the depositional units is based on microscopic studies of facbric, sedimentary structures, and clastic carbonate content (Karkanas et al., this issue).

The site was found ~30 m below the present, pre-mine operation surface, at an altitude of ~350 m above sea level (masl). The maximum elevation attained by the fluviolacustrine sediment in the basin was ~430–450 masl, sometime during the end of the Middle Pleistocene after which the basin opened due to regressive erosion by a neighbouring river basin and the modern drainage system was established. The clastic sedimentary sequence in the area of the site is developed between Lignite Seams II and III. The Matuyama/Brunhes palaeomagnetic boundary at 0.78 Ma is found in the upper part of the lowest Lignite Seam I (Okuda et al., 2002; Tourloukis et al., this issue), so sediments dated in this study must, therefore, be younger. Several studies of the lignite layers suggest that peat was forming during warm periods of the Pleistocene, whereas clastic sedimentation prevailed during cold periods (Nickel et al., 1996; Okuda et al., 2002; van Vugt et al., 2000). The Marathousa Member comprises a relatively continuous sedimentary sequence and according to the pollen-based climatostratigraphic model of Okuda et al. (2002) it probably spans isotopic stages 15–9. Alternative models have also been suggested, moving the sequence one interglacial up or down (van Vugt et al., 2000; Okuda et al., 2002). According to the age model preferred by Okuda et al. (2002), Marathousa I is placed in MIS 14 (~565–540 ka). A revised age model suggested by Tourloukis et al. (this issue) offers an alternative option that places the site in MIS 12 (~480–420 ka). The latter interpretation is more consistent with the single ESR age estimate of 370 ± 110 ka (2σ) presented for one of the uppermost lignite seams in Okuda et al. (2002).

3. Methods

3.1. Optical dating

Optical dating provides a means of determining burial ages for sediments and associated artefacts and fossils (Huntley et al., 1985; Aitken, 1998; Duller, 2004; Wintle, 2014; Roberts et al., 2015; Athanassas and Wagner, 2016). The method is based on the time-dependent increase in the number of trapped electrons induced in mineral grains—such as quartz and potassium-rich (K-rich) feldspar—by low levels of ionising radiation from the decay of natural uranium, thorium and potassium in the surrounding deposits, from within the mineral grains themselves, and from cosmic rays. The time elapsed since the light-sensitive electron traps were emptied can be determined from measurements of the luminescence signals from K-feldspar (infrared stimulated luminescence, IRSL, and post-infrared IRSL, pIRIR)—from which the equivalent dose (D_e) is estimated—together with determinations of the radioactivity of the sample and the material surrounding it to a distance of ~30 cm (the environmental dose rate). The luminescence 'clock' is reset by just a few hours (K-feldspar) of exposure to sunlight. The D_e divided by the environmental dose rate gives the burial time of the grains in calendar years ago.

3.2. Sample collection

We visited the field site and collected a total of 9 samples from excavation areas A and B at elevations of between 349 and 353 masl. We deliberately targeted the sandier layers with the lowest environmental dose rates as those samples will give us the highest chance of dating success. These samples also maximised our chances in finding sand-sized (> 90 μm diameter) grains of K-feldspar that were generally quite rare and limited the number of multigrain aliquots that could be measured for each sample. We also used the opportunity to directly measure the gamma dose rate *in situ*. The stratigraphic sequences for both areas are shown in Fig. 1, together with photographs of the 7 samples collected for which ages could be calculated. The stippled lines show the relationship between the major stratigraphic units between the two excavation areas. We were unable to extract enough sand grains from a sample collected from a sandy layer inside the sequence of Lignite seam III, and this sample remains undated.

The location of sample CHO-SU3 is not depicted in the stratigraphy of Fig. 1 as it comes from a higher stratigraphic level, the Megalopolis Member, at an elevation of ~362 masl and from a different mine area—Choremi mine, ~2 km to the south of Marathousa 1. The site represents a small concentration of lithics found during a directed survey of the Megalopolis basin (Thompson et al., this issue). Unfortunately, during a large slumping event in the mine, the site was destroyed, but a sample (CHO-SU3) for luminescence dating was collected prior to this event. We present here the age of this sample as it offers a useful chronological point in the interpretation of the age of the

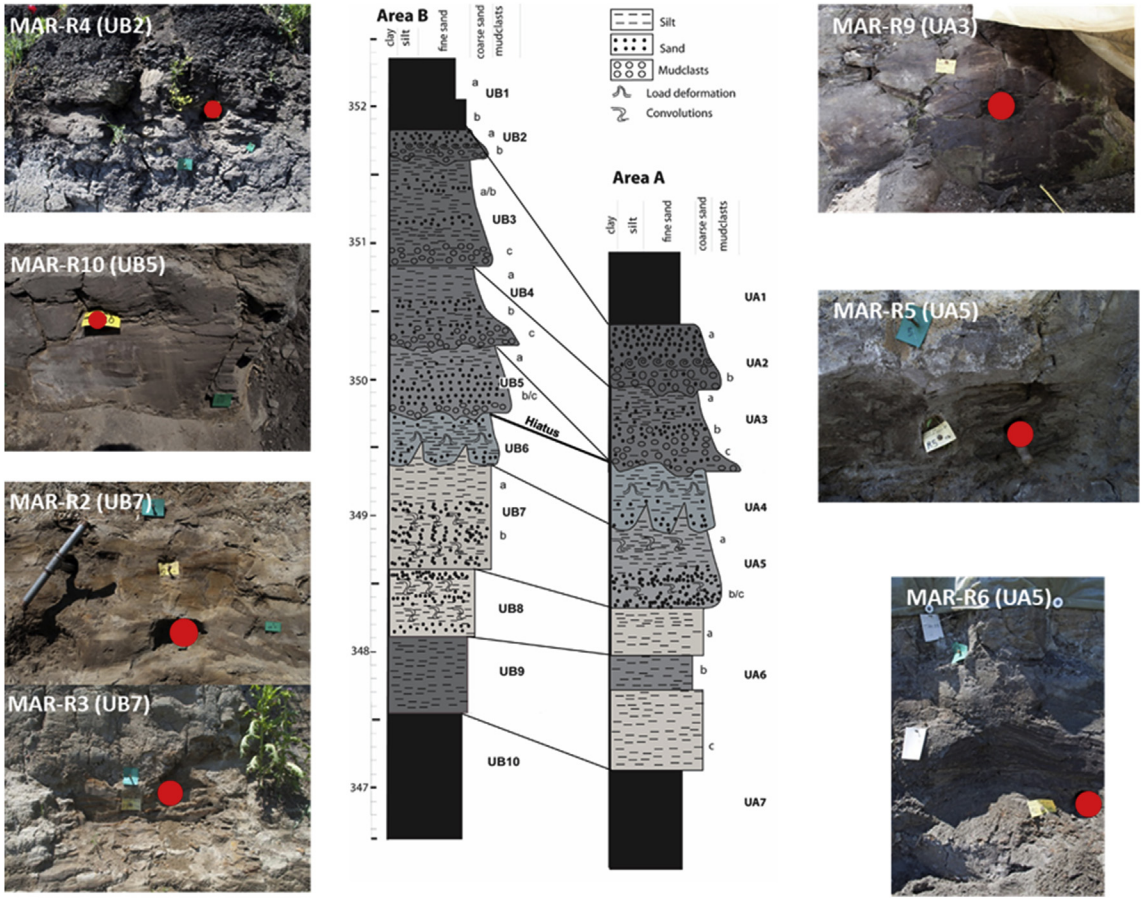

Fig. 1. Stratigraphic sediment logs for two different excavation areas (Area A and Area B) located ~60 m apart and the sedimentary units. Correlation between the two areas is based on sedimentary fabric, structure, and carbonate and organic content. See text for more information. Photographs of sedimentary contexts from which luminescence dating samples were collected (indicated by red filled circles) are also shown. The archaeological finds are concentrated on the boundaries of UB5-UB4 and UA4-UA3. (For interpretation of the references to colour in this figure legend, the reader is referred to the Web version of this article.)

basin.

3.3. Sample preparation

All of the samples were prepared using routine optical dating procedures (Aitken, 1998). Samples were first treated with HCl acid and H_2O_2 solution to remove carbonates and organic matter, respectively. The remaining sediment was then dried and sieved to obtain a range of sand-sized grain fractions. Grains of 180–212 μm in diameter were used for dating of 5 of the 7 samples. Grains of between 90–150 and 90–125 μm in diameter were used for samples MAR-R3 and MAR-R4, respectively. The K-feldspar grains were separated from quartz and heavy minerals using sodium polytungstate solutions of densities 2.62 and 2.58 g/cm^3. The K-feldspar grains were immersed in 10% HF acid for 40 min to etch the surfaces of the grains and remove the outer, alpha-irradiated portions. The HF-etched feldspar grains were then rinsed in HCl acid to remove any precipitated fluorides and sieved again.

3.4. Equivalent dose (D_e) measurements

The D_e values for K-feldspar grains were determined using multiple-aliquot pIRIR measurements (Li et al., 2017). The pIRIR measurements were made on an automated Risø TL-DA-20 luminescence reader equipped with infrared (870 nm) light-emitting diodes (LEDs) for stimulation of multi-grain aliquots (Bøtter-Jensen et al., 2003). Luminescence emissions were detected using an Electron Tubes Ltd 9235QA photomultiplier tube. The pIRIR emissions were detected through Schott BG-39 and Corning 7–59 filters. The multi-grain aliquot measurements were made using 9.8 mm-diameter stainless steel discs, to which grains were affixed to a 5 mm-diameter spot in the centre of each disc using 'Silkospray' silicone oil. Irradiations were carried out inside the luminescence reader using a $^{90}Sr/^{90}Y$ beta source that has been calibrated using a range of known gamma-irradiated quartz standards. Solar bleaching was conducted using a Dr Hönle solar simulator (model: UVACUBE 400).

A multiple-aliquot regenerative-dose (MAR) procedure (Li et al., 2017) was used to measure all samples from Marathousa 1 and Choremi. This method was developed specifically for these samples and is based on the so-called multiple-aliquot pre-dose multiple-elevated-temperature pIRIR (pMET-pIRIR) procedure for K-feldspar (Li et al., 2013, 2014b), which appear to be immune from fading (Li and Li, 2011; Li et al., 2014a). Furthermore, the MAR method has some advantages over the SAR method in overcoming problems associated with inappropriate sensitivity correction of the natural signal (L_n) and its associated test dose signal (T_n) (Chen et al., 2015; Guo et al., 2015; Li et al., 2017) and, combined with a standardised growth curve (SGC) approach, can also significantly reduce instrument time.

The MAR procedure for K-feldspar is based on the establishment of a SGC constructed from the re-normalised L_x/T_x signals of multiple groups of aliquots (Li et al., 2017). We have shown that the MAR dose response curve of the pMET-pIRIR signal continues to grow with dose beyond 1500 Gy, without reaching saturation, and that a SGC exists for our samples (see Li et al., 2017 for details). We, therefore, calculated D_e values for all the samples based on the MAR SGCs established using 4 of the samples—MAR-01, MAR-R1, MAR-R2 and MAR-R5. For each

sample, after measuring their L_n and T_n signals, each aliquot was bleached for ~4 h in the solar simulator and then given a regenerative dose of 400 Gy and a subsequent test dose of 60 Gy, the same values used to establish the MAR SGCs. The L_n/T_n ratios were then re-normalised using the corresponding (L_r/T_r) ratios, and the re-normalised ratios ($\frac{L_n / T_n}{L_r / T_r}$) at each stimulation temperature were then calculated using the central age model (Galbraith et al., 1999; Galbraith and Roberts, 2012) to obtain weighted-mean values. These weighted-mean ($\frac{L_n / T_n}{L_r / T_r}$) values were then projected onto the MAR SGCs to estimate the D_e values. Full details of the method and experimental procedures and tests are provided in Li et al. (2017).

3.5. Environmental dose rate measurements

The total environmental dose rate consists of contributions from beta, gamma and cosmic radiation external to the grains, plus a beta dose rate due to the radioactive decay of potassium (^{4}K) and rubidium (^{87}Rb) inside sand-sized grains of K-feldspar. To calculate the optical ages, we have assumed that the present-day radionuclide activities and dose rates have prevailed throughout the period of sample burial. As shown by experiments and modelling, most time-dependent disequilibria in the uranium and thorium decay chains are unlikely to give rise to errors in the total dose rate of more than a few percent when emission-counting methods—such as those used in this study—are used to measure the external beta and gamma dose rates (Olley et al., 1996, 1997).

We estimated the beta dose rates directly by low-level beta counting of dried, homogenised and powdered sediment samples in the laboratory, using a Risø GM-25-5 multi-counter system (Bøtter-Jensen and Mejdahl, 1988). We prepared and measured samples, analysed the resulting data, and calculated the beta dose rates and their uncertainties following the procedures described and tested in Jacobs and Roberts (2015); three sub-samples were measured for each sample. For all samples, allowance was made for the effect of water content (Nathan and Mauz, 2008), grain size (Brennan, 2003) and HF acid etching (Bell and Zimmerman, 1978) on beta-dose attenuation.

Gamma dose rates were measured directly by *in situ* gamma spectrometry to take into account any spatial heterogeneity in the gamma radiation field within 30 cm of each sample. The gamma dose rate was measured at every sample location. Counts were collected for 30 min with a NaI(Tl) detector (2-inches in diameter). The detectors were calibrated using the concrete blocks at Oxford University (Rhodes and Schwenninger, 2007) and the gamma dose rates were determined using the 'threshold' technique (Mercier and Falguères, 2007).

We ignored the cosmic-ray contribution to the dose rate, because the influence of cosmic radiation on the minerals is completely attenuated by the overlying sediment that are > 30 m in depth.

K-feldspar also has a significant internal beta dose rate from the radioactive decay of ^{4}K and ^{87}Rb inside the grains. To calculate the internal beta dose rates for K-feldspar grains of different sizes, we combined the estimates for ^{4}K (12 ± 1%; Huntley and Baril, 1997) and ^{87}Rb (400 ± 100 μg/g; Huntley and Hancock, 2001), and used the conversion factors of Liritzis et al. (2013) and a correction for the absorbed dose fraction, which varies depending on grain size. For K-feldspar grains of 180–212 μm and 90–125 μm in diameter, for example, the effective internal beta dose rates are 0.83 ± 0.10 and 0.48 ± 0.06 Gy/ka, respectively.

3.6. Moisture content estimation

Both the beta and gamma dose rates are affected by moisture content and allowance should be made for the attenuation due to moisture content (Nathan and Mauz, 2008). Individual measured current water contents for each of the samples range between ~9% and 38% (Table 1), but these were measured for samples collected from variably dried out section walls and are thought to represent significant underestimates of the average water content experienced over the burial history of the samples. Freshly dug trenches during excavation at Marathousa revealed generally wet sediment even during the dry months. Note that excavations are conducted adjacent to an old lignite mine bench and, therefore, some water draining must have occurred in the recent past. In the Kyparissia mine, to the north of the Marathousa mine, the water table was found at ~330–340 masl and in several other areas up to ~350–380 masl (Tisiftsis, 1991). Marathousa 1 is located at ~350 masl, so we assume that the sediments at Marathousa 1 were water-saturated and that this was the situation for their entire burial history.

A simple experiment was carried out to estimate the maximum water-holding capacity of the sediment. Small rectangular sediment blocks (5 × 5x5 cm) were extracted from the areas where luminescence samples were collected (Fig. 1). Samples were dried at 105 °C for 24 h. Their bulk volume (V_t) was measured precisely with 3D laser scanning (Next Engine). They were then dried again to eliminate the possibility that the sediment have gained back humidity during scanning. The sediment were weighed (M_d) and their dry bulk density estimated ($\rho_d = M_d/V_t$). The dried samples were placed in beakers, partially filled with distilled water, weighed, and left overnight for all the voids to be filled with water. Care was taken to ensure that enough water was available to saturate the sample through capillary action. Samples were not completely immersed in water as some trapped air could block water penetration. Due to the very low clay content of samples, voids were easily filled with water. This was tested with breaking some extra test samples and confirming that they were completely soaked with water. After pouring out excess water, the beakers with the samples were weighed again and the wet sample weight (M_w) was estimated after extracting the weight of the beaker. As the density of distilled water is 1 g/cm^3 the difference between dry and wet sample weight equals the pore volume of the samples. Porosity was calculated using equation (1):

$$\text{Porosity } \% = [(M_w - M_d)/M_d] \times 100 \quad (1)$$

To check the validity of the pore space volume approach in evaluating water content, we also calculated porosity using equation (2):

$$\text{Porosity} = (1 - \text{dry bulk density } (\rho_d) / \text{particle density } (\rho_p)) \times 100 \quad (2)$$

Inorganic sediment particle density is in the range 2.6–2.7 g/cm^3 and conventionally taken as 2.65 g/cm^3 (Blake and Hartge, 1986; Boyd, 1995). The average particle density of sediment containing a significant fraction of organic particles can be corrected assuming a density of 1.25 g/cm^3 for organic matter (OM) (Boyd, 1995). Organic content values have been estimated by Loss on Ignition (LOI) of samples at 450 °C (Karkanas et al., this issue) and are presented in Table 1. Therefore, the weighted mean sediment particle density (g/cm^3) = [1.25(%OM) + 2.65(100%-%OM)] (Avnimelech et al., 2001). For dry bulk density the experimentally determined value were used. Porosity was then estimated using equation (2).

Porosity was also calculated using the equation of dry bulk density by Avnimelech et al. (2001) for organic-rich flooded sediment using equation (3), with porosity estimated using equation (2):

$$\rho_d = 1.776 - 0.363 \text{ Log}_e \text{ OC} \quad (3)$$

In which OC = organic carbon = OM/1.7.

Table 1 shows the experimentally determined and calculated porosities using equations (1)–(3) above.

The effect of compaction on porosity, and as a consequence, on water content is more difficult to address. The sediments at Marathousa 1 were deposited under water and buried under deposited sediment gradually reaching a maximum thickness of ~100 m. Paul and Barras (1998) found that for the simple case of self-weight compression of the

Table 1
Water content estimation of luminescence samples collected from Marathousa 1 and Choremi, Megalopolis Basin.

Sample	Unit	OM %	Current Meas. Water content %	Porosity Meas. % (1)	Porosity Calc. % (2)	Porosity Calc. % (3)	Porosity Uncomp. % (4)	Porosity Uncomp. % (5)	Porosity Burial Averaged % (6)
CHO-SU3	–	1.11	6	40	38	27	43	-[a]	42
R4	UB2a	21.7	38	64	58	64	85	80	75
R9	UA3b	11.3	35	52	49	56	76	65	64
R01/10	UB5	8.0	15	44	45	53	70	56	57
R2	UB7	3.8	9	45	39	43	55	45	50
R3	UB7	3.8	9	45	41	43	55	45	50
R5	UA5	4.5	9	48	49	45	57	45	53
R6	UA5	3.5	16	46	49	40	52	42	49

OM = organic matter.
(1)Porosity measured experimentally.
(2)Porosity calculated on basis of the dilution of inorganic sediment (d = 2.65) with organic matter (d = 1.25).
(3)Porosity calculated based on Avnimelech et al. (2001).
(4)Porosity calculated for uncompacted samples based on van Asselen (2011).
(5)Porosity calculated for uncompacted samples based on Bartholdy et al. (2010).
(6)Averaged burial porosity based on (1) and (4).
[a] Negative value – this equation seems not to work for such a low organic content.

layer thickness for incompressible materials, such as sand and silt, it is only ~1–2%. The sandy sediments of the samples at Marathousa 1, below the layers with the archaeological remains fall into this category, and we can safely assume that compaction did not play a significant role in water content. However, the layers containing and overlying the archaeological remains are particularly rich in compressible organic matter.

One way of calculating the original porosity of the organic-rich sediment is to use equation (4) for estimating dry density (uncompacted) as suggested by van Asselen (2011) for peat compaction:

$$\rho_d = a - ce^{-(b/OM)} \quad (4)$$

In which a = 1.5; b = 6; c = 1.53.

And then to substitute in equation (2) for porosity. The amount of porosity so estimated is higher by between 6 and 25%, with the highest differences observed for the organic-rich sediment samples (Table 1).

An alternative approach is offered by Bartholdy et al. (2010) who, in addition to OM, take into account the amount of incompressible sand in estimation of autocompaction of silty marsh clays. In this case, dry bulk density is estimated using equation (5):

$$44478 \times OM^{-0.73} \times 0.98 \times S^{0.036} \quad (5)$$

In which S is the amount of sand in the sediment (values were used from Sifogeorgaki and Karampatsou, 2014).

The calculated uncompacted porosities are lower than the ones produced using the van Asselen (2011) approach, but still higher than our measured values. They also show the same pattern with respect to OM content (Table 1) in agreement with Paul and Barras (1998) who suggested that pure sands and silts are practically uncompressible.

4. Results

4.1. Equivalent dose (D_e) values

The D_e values are plotted as a function of stimulation temperature in Fig. 2 (D_e-T plots) for all the samples. For most of the samples, the MAR D_e values differ negligibly with stimulation temperature, implying that there is very little difference in fading rate of the signals measured at the various stimulation temperatures. This has been supported by the anomalous fading tests made on samples MAR-R2 and MAR-R5, which showed that there is little difference between the fading rates for the various signals stimulated at different temperatures and all the fading rates are statistically consistent with zero at 2σ (see Li et al., 2017 for details). We are, therefore, confident that finite and reliable D_e values were obtained for these samples based on the 275 °C pMET-pIRIR signals. The final D_e values used for calculation of the ages are provided in Table 2.

4.2. Environmental dose rate estimates

To calculate the final beta and gamma dose rates, the measured values need to be corrected for the average burial water content. The uncompacted sediment porosities calculated as (4) and (5) in Table 1 is only appropriate for sedimentary material close to the original surface of the deposit. These values should, therefore, be considered maxima as they are not representative of the entire burial history of the samples. A more likely and representative time-averaged burial porosity value is somewhere between the present measured porosities ((1) in Table 1) and that calculated for uncompacted deposits ((4) in Table 1); this average is provided as (6) in Table 1. We corrected the beta and gamma dose rates of all samples for water content using two different approaches (Table 2): a) using the measured water content for the whole burial time ((1) in Table 1), and b) the average measured content and maximum compaction values obtained using the approach of van Asselen (2011) ((6) in Table 1). The environmental dose rates so calculated are presented in Table 2 with our preferred estimates based on the second approach highlighted in grey in Table 2. The organic-rich layers are obviously affected more because of the greater extend of compaction. The beta and gamma dose rates calculated using the two different approaches differ between ~9% (MAR-R10) and 1.5% (CHO-SU3) and on average ~5%.

The estimated gamma and beta dose rates for the 8 samples are provide in Table 2. The gamma dose rates measured directly in the field are quite reproducible between the different samples ranging from 0.45 ± 0.04 (MAR-R5) to 0.63 ± 0.05 (MAR-R3) Gy/ka. The beta dose rates show greater variability, ranging from 0.47 ± 0.04 (MAR-R5) to 0.82 ± 0.07 (MAR-R10) Gy/ka, with the organic-rich layers having the highest beta dose rates. The total dose rates range from 1.50 ± 0.10 (MAR-R4) to 2.24 ± 0.13 (MAR-R10) Gy/ka (Table 2).

4.3. Age estimates and discussion

The final pIRIR ages for all samples, calculated using the two alternative water content values discussed above, are listed in Table 2, together with the supporting D_e and dose rate estimates. Values highlighted in grey represent our preferred estimates. Uncertainties on the ages are given at 1σ (the standard error on the mean) and were estimated by combining, in quadrature, all known and estimated sources of random and systematic error. Ages are presented in stratigraphic order. The age obtained for the single sample from Choremi is 264 ± 22 ka,

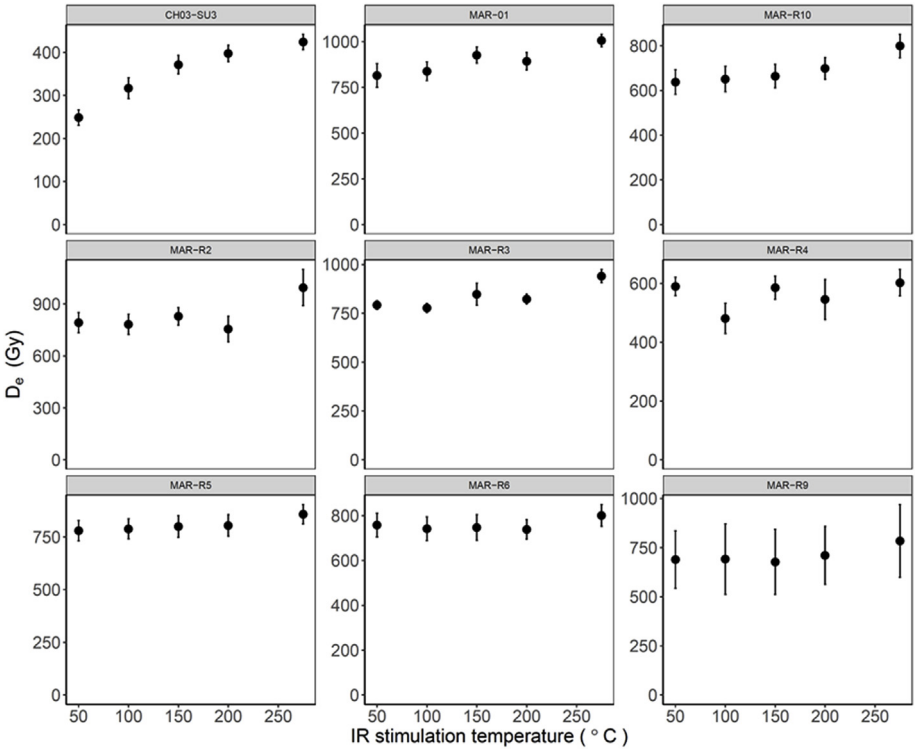

Fig. 2. D_e values obtained based on MAR SGC (circles) plotted against IR stimulation temperature for all samples measured in this study.

Table 2
Dose rate data, D_e values and OSL ages for 1 sediment sample from Choremi mine and 8 sediment samples from Marathousa 1. Age were calculated for two alternative water content calculations (see Table 1 and text).

Sample	Excavation unit	Water content (%)	External dose rate (Gy/ka)		Internal dose rate (Gy/ka)	Total dose rate (Gy/ka)	D_e value (Gy)	Age (ka)
			Gamma	Beta				
CHO-SU3		40	0.37 ± 0.03	0.60 ± 0.04	0.66 ± 0.09	1.63 ± 0.11	426 ± 23	262 ± 22
		42	0.36 ± 0.03	0.59 ± 0.05		1.61 ± 0.11		264 ± 22
MAR-R4	UB2a	64	0.53 ± 0.05	0.56 ± 0.05	0.48 ± 0.06	1.57 ± 0.10	622 ± 55	396 ± 43
		75	0.49 ± 0.05	0.52 ± 0.05		1.50 ± 0.10		415 ± 46
MAR-R9	UA3b	52	0.65 ± 0.05	0.79 ± 0.07	0.83 ± 0.10	2.26 ± 0.13	816 ± 88	361 ± 45
		64	0.60 ± 0.05	0.72 ± 0.07		2.15 ± 0.13		380 ± 48
MAR-R10	UB5	44	0.65 ± 0.05	0.91 ± 0.07	0.83 ± 0.10	2.38 ± 0.13	884 ± 47	371 ± 29
		57	0.59 ± 0.05	0.82 ± 0.07		2.24 ± 0.13		394 ± 32
MAR-01	UB5	44	0.75 ± 0.07	0.92 ± 0.07	0.83 ± 0.10	2.50 ± 0.14	1124 ± 58	451 ± 35
		57	0.68 ± 0.07	0.84 ± 0.07		2.34 ± 0.14		480 ± 39
MAR-R2	UB7	45	0.58 ± 0.05	0.68 ± 0.06	0.83 ± 0.10	2.08 ± 0.12	940 ± 56	452 ± 39
		50	0.55 ± 0.04	0.65 ± 0.05		2.03 ± 0.12		462 ± 40
MAR-R3	UB7	45	0.66 ± 0.05	0.76 ± 0.06	0.66 ± 0.09	2.08 ± 0.12	959 ± 35	462 ± 33
		50	0.63 ± 0.05	0.73 ± 0.06		2.02 ± 0.12		474 ± 35
MAR-R5	UA5	48	0.46 ± 0.04	0.49 ± 0.04	0.83 ± 0.10	1.78 ± 0.11	887 ± 44	498 ± 41
		53	0.45 ± 0.04	0.47 ± 0.04		1.75 ± 0.11		508 ± 42
MAR-R6	UA5	48	0.59 ± 0.05	0.58 ± 0.05	0.83 ± 0.10	1.99 ± 0.12	855 ± 50	428 ± 37
		53	0.57 ± 0.05	0.56 ± 0.05		1.95 ± 0.12		438 ± 38

consistent with deposition during oxygen isotope stage (OIS) 8. At Marathousa 1, ages of between 380 ± 48 ka (MAR-R9) and 480 ± 39 ka (MAR-01) were obtained for the units containing and overlying the artefacts and fossils (samples MAR-R4, R9, R10 and 01). Ages of between 438 ± 38 ka (MAR-R6) and 508 ± 42 ka (MAR-R5) were obtained for the units underlying the artefacts and fossils (samples MAR-R2, R3, R5 and R6). As all samples from the lower part of the sequence come from the same stratigraphic level (UA5 and UB7), we have calculated a weighted average age of 470 ± 30 ka. When using the lower water content values based on the burial average porosity values provided as (1) in Table 1, a weighted mean estimate of 460 ± 28 ka is calculated. This age is statistically indistinguishable from our preferred estimates. The biggest difference in age using the two different water content scenarios is observed for the organic-rich samples (MAR-R4, R9, R10 and 01) that show a 5–6% increase in age with use of the higher water content values. Ages for the sandier layers from the lower part of the sequence only increase by 2–2.5%, confirming that these sediments are practically uncompressible. The same is also true for samples CHO-SU3 where the age is not affected by the water content change due to compression during burial.

Overall, there is good agreement and reproducibility between ages for samples from the same units. The standard errors associated with the ages are relatively large, ranging between 7% and 12.5% at 1 sigma and should be taken into account when ages are assigned to oxygen isotope stages and a chronological sequence inferred from these ages.

A major depositional hiatus and erosional event between correlated

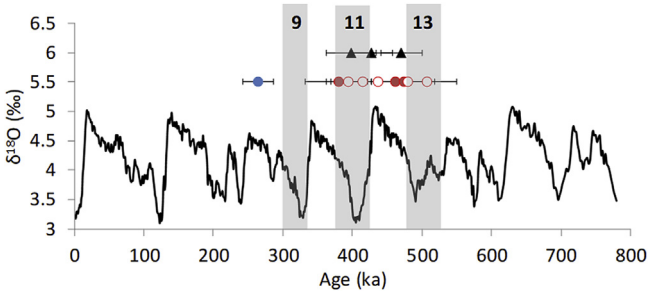

Fig. 3. Individual age estimate with 1 sigma uncertainties plotted above the oxygen isotope curve (Lisiecki and Raymo, 2005) for the last 780 ka. The blue filled circle represent the age for the single sample from Choremi mine and the open and filled red circles represent ages from excavation areas B and A, respectively, from Marathousa1. The filled black triangles represent weighted mean age estimates for samples from units below and above the archaeological and palaeontological units and the unit on the surface of which the latter is found (UB5). The grey shaded bands represent the three interglacial periods most closely associated with the ages obtained in this study. (For interpretation of the references to colour in this figure legend, the reader is referred to the Web version of this article.)

units UA4 and UB6 (Fig. 1) and the overlying sediments was identified based on the sedimentary and microstratigraphic analysis of the site (Karkanas et al., this issue). A considerable temporal hiatus is not supported by a statistically significant time gap, because of the coarser resolution of the chronology compared to the stratigraphic observations.

The ages and their 1-sigma uncertainties are plotted above the oxygen isotope curve in Fig. 3. The age in blue represents sample CHO-SU3 and the filled and open red symbols those from excavation areas A and B at Marathousa 1, respectively. Sediment deposition coincides with OIS 13 to 11 for Marathousa I and OIS 8 for Choremi. Also shown in Fig. 3 are black triangles that represent three weighted mean age estimates: The youngest age is the combined age estimate for samples overlying the archaeological and palaeontological deposits (UB2a and UA3b; Fig. 1), the middle estimate represents UB5 and the oldest age estimate for those deposits underlying the major sedimentary hiatus (UA5 and UB7; Fig. 1). Previous lithostratigraphic and palynostratigraphic studies and available age models, assigned the whole sediment sequence lying between Lignite seams III and II (upper and lower black units, respectively in Fig. 1) to one glacial period, with the two lignite deposits belonging to two separate and major interglacials (van Vugt et al., 2000; Okuda et al., 2002). Based on the weighted mean age estimates (black triangles in Fig. 3), the pMET-pIRIR ages place the lower part of the sequence in OIS 12 (glacial), the deposit associated with the archaeological materials at the boundary between OIS 12 and OIS 11, and the upper part in OIS 11 (interglacial). Given the overall uncertainty associated with each individual age, and specifically the uncertainty of our water content estimations and the burial and compaction history of especially the upper part of the sequence consisting of organic-rich deposits, it is likely that the upper part of the sequence could be placed at the end of OIS12/beginning of OIS11. These MAR pMET-pIRIR ages presented here are consistent with one of the existing age models – the one presented by Tourloukis et al. (this issue) and are in broad agreement with the preliminary ESR ages presented by Blackwell et al. (2016).

Sample CHO-SU3 was collected from the overlying Megalopolis Member and gave an age of ~260 ka, which is consistent with deposition during OIS 8. The age is not affected by the water content changes due to compression during burial. The age is in good agreement with the overall stratigraphy of the basin and with the available age models. It was previously suggested that the Megalopolis Member was deposited after OIS 9 (Okuda et al., 2002; cf. Tourloukis et al., this issue).

5. Conclusions

Obtaining luminescence ages for the deposits from Marathousa 1 posed several challenges. Experimental and analytical work resulted in the development of a multiple aliquot measurement procedure based on the pIRIR signal from k-feldspar grains (Li et al., 2017). Since these sediments were deposited on a lake margin and heavily influenced by lake-level fluctuations over its entire burial history, a detailed investigation of the palaeo-water content of the site was required. This involved different ways of measuring and estimating past and present water content, and calculation of porosity and the effect of compaction to provide a best-guess estimate of the time-average water content of these samples. Different samples with different compositions (sandy vs. organic-rich) were more or less sensitive to these calculations. The effect on the environmental dose rate was more significant for the organic-rich sediment. Uncertainty still remain about the effect of possible disequilibrium in the uranium decay series as this was not explicitly addressed in this study.

The new set of luminescence ages reported here for Marathousa 1 were collected from two separate excavation areas and support the stratigraphic correlations that were made between the two areas (Karkanas et al., this issue). Ages are not in strict stratigraphic order, but the relatively large age uncertainties should be kept in mind. Ages are consistent with sediment deposition during OIS 12 and OIS 11 and support the age model proposed by Tourloukis et al. (this issue), who suggest that lignite seams II and III were deposited during the interglacial periods of OIS 13 and OIS 11, respectively, and that the intervening clastic-rich deposit dated in this study, was deposited during the glacial period of OIS 12. The archaeological and palaeontological deposits at Marathousa I, therefore, date to OIS 12.

Acknowledgements

This research was funded by the Australian Research Council through Future Fellowships to Jacobs (FT150100138) and Li (FT140100384). Yasaman Jafari and Terry Lachlan provided valuable support in the laboratory. The archaeological research at Marathousa 1 was supported by the European Research Council (ERC StG no. 283503 “PaGE”: Paleoanthropology at the Gates of Europe: Human evolution in the southern Balkans, and ERC Consolidator Grant no. 724703, “Human evolution at the crossroads”, awarded to K. Harvati). We are grateful to the excavation teams that worked in the Marathousa-1 site from 2013 to 2017. We thank the Ministry of Culture, the authorities of the Peloponnese Prefecture and the Municipality of Megalopolis and the Public Power Corporation S. A. Hellas for their support throughout this work.

Appendix A. Supplementary data

Supplementary data related to this article can be found at http://dx.doi.org/10.1016/j.quaint.2018.06.029.

References

Aitken, M.J., 1998. An Introduction to Optical Dating. Oxford University Press, Oxford.
Athanassas, C.D., Wagner, G.A., 2016. Geochronology beyond radiocarbon: optically stimulated luminescence dating of palaeoenvironments and archaeological sites. Elements 12, 27–32.
Avnimelech, Y., Ritvo, G., Meijer, L.E., Kochba, M., 2001. Water content, organic carbon and dry bulk density in flooded sediments. Aquacult. Eng. 25, 25–33.
Bartholdy, J., Pedersen, J.B.T., Bartholdy, A.T., 2010. Autocompaction of shallow silty salt marsh clay. Sediment. Geol. 223, 310–319.
Bell, W.T., Zimmerman, D.W., 1978. The effect of HF acid etching on the morphology of quartz inclusions for thermoluminescence dating. Archaeometry 20, 63–65.
Blake, G.R., Hartge, K.H., 1986. Bulk density. In: Klute, A. (Ed.), Methods of Soil Analysis, Part 1, Physical and Mineralogical Methods. American Society of Agronomy, Madison, Wisconsin, USA, pp. 363–375.
Blackwell, B.A.B., Singh, I., GopalKrishna, K., Chen, K.K., Sakhrani, N., Tourloukis, V., Karkanas, P., Florentin, J.I.B., Panagopoulou, E., Harvati, K., Skinner, A., 2016. ESR

dating the fossil-bearing layers at the Marathousa 1 site. In: Paleoanthropological Society Meeting, Atlanta. PaleoAnthropology, pp. A4–A5.
Bøtter-Jensen, L., Mejdahl, V., 1988. Assessment of beta-dose-rate using a GM multi-counter system. Nucl. Tracks Radiat. Meas. 14, 187–191.
Bøtter-Jensen, L., Andersen, C.E., Duller, G.A.T., Murray, A.S., 2003. Developments in radiation, stimulation and observation facilities in luminescence measurements. Radiat. Meas. 37, 535–541.
Boyd, C.E., 1995. Bottom Soils, Sediment, and Pond Aquaculture. Chapman & Hall, New York.
Brennan, B.J., 2003. Beta doses to spherical grains. Radiat. Meas. 37, 299–303.
Chen, Y., Li, S.-H., Li, B., Hao, Q., Sun, J., 2015. Maximum age limitation in luminescence dating of Chinese loess using the multiple-aliquot MET-pIRIR signals from K-feldspar. Quat. Geochronol. 30, 207–212.
Duller, G.A.T., 2004. Luminescence dating of Quaternary sediments: recent advances. J. Quat. Sci. 19, 183–192.
Galbraith, R.F., Roberts, R.G., 2012. Statistical aspects of equivalent dose and error calculation and display in OSL dating: an overview and some recommendations. Quat. Geochronol. 11, 1–27.
Galbraith, R.F., Roberts, R.G., Laslett, G.M., Yoshida, H., Olley, J.M., 1999. Optical dating of single and multiple grains of quartz from Jinmium rock shelter, northern Australia: Part I, experimental design and statistical models. Archaeometry 41, 339–364.
Guo, Y.J., Li, B., Zhang, J.F., Roberts, R.G., 2015. Luminescence-based chronologies for Palaeolithic sites in the Nihewan Basin, northern China: first tests using newly developed optical dating procedures for potassium feldspar grains. J. Archaeol. Sci.: Report 3, 31–40.
Harvati, K., 2016. Paleoanthropology in Greece: recent findings and interpretations. In: Harvati, K., Roksandic, M. (Eds.), *Paleoanthropology of the Balkans and Anatolia: Human Evolution and its Context.* Vertebrate Paleobiology and Paleoanthropology Series. Springer, Dordrecht, pp. 3–14.
Huntley, D.J., Godfreysmith, D.I., Thewalt, M.L.W., 1985. Optical dating of sediments. Nature 313, 105–107.
Huntley, D.J., Baril, M.R., 1997. The K Content of the K-feldspars Being Measured in Optical Dating or in Thermoluminescence Dating. Ancient TL, vol. 15. pp. 11–13.
Huntley, D.J., Hancock, R.G.V., 2001. The Rb contents of the K-feldspars being measured in optical dating. Ancient TL 19, 43–46.
Jacobs, Z., Roberts, R.G., 2015. An improved single grain OSL chronology for the sedimentary deposits from Diepkloof Rockshelter, Western Cape, South Africa. J. Archaeol. Sci. 63, 175–192.
Karkanas, P. Tourloukis, V., Thompson, N., Giusti, D., Panagopoulou, E., Harvati, K., in this issue. Sedimentology and micromorphology of the lower palaeolithic lakeshore site Marathousa 1, Megalopolis Basin, Greece. Quat. Int.
Konidaris, G.E., Athanassiou, A., Tourloukis, V., Thompson, N., Giusti, D., Panagopoulou, E., Harvati, K., in this issue. The Elephas (Palaeoloxodon) antiquus skeleton and other large mammals from the Lower Palaeolithic locality Marathousa-1 (Megalopolis Basin, Greece): preliminary results on taxonomy, biochronology, palaeoecology and taphonomy. Quat. Int.
Li, B., Li, S.-H., 2011. Luminescence dating of K-feldspar from sediments: a protocol without anomalous fading correction. Quat. Geochronol. 6, 468–479.
Li, B., Jacobs, Z., Roberts, R.G., Li, S.-H., 2013. Extending the age limit of luminescence dating using the dose-dependent sensitivity of MET-pIRIR signals from K-feldspar. Quat. Geochronol. 17, 55–67.
Li, B., Jacobs, Z., Roberts, R.G., Li, S.-H., 2014a. Review and assessment of the potential of post-IR IRSL dating methods to circumvent the problem of anomalous fading in feldspar luminescence. Geochronometria 41, 178–201.
Li, B., Roberts, R.G., Jacobs, Z., Li, S.-H., 2014b. A single-aliquot luminescence dating procedure for K-feldspar based on the dose-dependent MET-pIRIR signal sensitivity. Quat. Geochronol. 20, 51–64.
Li, B., Jacobs, Z., Roberts, R.G., 2017. An Improved Multiple-aliquot Regenerative-dose (MAR) Procedure for post-IR IRSL Dating of K-feldspar. Ancient TL, vol. 35. pp. 1–10.
Liritzis, I., Stamoulis, K., Papachristodoulou, C., Ioannides, K., 2013. A re-evaluation of radiation dose-rate conversion factors. Mediterranean Archaeology and Archaeometry 13, 1–15.
Lisiecki, L.E., Raymo, M.E., 2005. A Pliocene-Pleistocene stack of 57 globally distributed benthic ^{18}O records. Paleoceanography 20, PA1003.
Mercier, N., Falguères, C., 2007. Field Gamma Dose-rate Measurement with a NaI(Tl) Detector: Re-evaluation of the "threshold" Technique. Ancient TL, vol. 25. pp. 1–4.
Nathan, R.P., Mauz, B., 2008. On the dose-rate estimate of carbonate-rich sediments for trapped charge dating. Radiat. Meas. 43, 14–25.
Nickel, B., Riegel, W., Schönherr, T., Velitzelos, E., 1996. Environments of coal formation in the Pleistocene lignite at Megalopolis, Peloponnesus (Greece) – reconstructions from palynological and petrological investigations. Neues Jahrbuch Geol. Palaontol. Abhand. 200, 201–220.
Okuda, M., van Vugt, N., Nakagawa, T., Ikeya, M., Hayashida, A., Yasuda, Y., Setoguchi, T., 2002. Palynological evidence for the astronomical origin of lignite-detritus sequence in the middle Pleistocene Marathousa member, Megalopolis, sw Greece. Earth Planet Sci. Lett. 201, 143–157.
Olley, J.M., Murray, A.S., Roberts, R.G., 1996. The effects of disequilibria in the uranium and thorium decay chains on burial dose rates in fluvial sediments. Quat. Sci. Rev. 15, 751–760.
Olley, J.M., Roberts, R.G., Murray, A.S., 1997. Disequilibria in the uranium decay series in sedimentary deposits at Allen's Cave, Nullarbor Plain, Australia: implications for dose rate determinations. Radiat. Meas. 27, 433–443.
Panagopoulou, E., Tourloukis, V., Thompson, N., Athanassiou, A., Tsartsidou, G., Konidaris, G.E., Harvati, K., 2015. Marathousa 1: a new Middle Pleistocene archaeological site from Greece. Antiquity 343 (Project Gallery).
Panagopoulou, E., Tourloukis, V., Thompson, N., Karkanas, P., Harvati, K., in this issue. The lower palaeolithic site of Marathousa 1, Megalopolis, Greece: overview of the evidence. Quat. Int.
Paul, M.A., Barras, B.F., 1998. A geotechnical correction for post-depositional sediment compression: examples from the Forth valley, Scotland. J. Quat. Sci. 13, 171–176.
Rhodes, E.J., Schwenninger, J.-L., 2007. Dose Rates and Radioisotope Concentrations in the concrete Calibration Blocks at Oxford. Ancient TL, vol. 25. pp. 5–8.
Roberts, R.G., Jacobs, Z., Li, B., Jankowski, N.R., Cunningham, A.C., Rosenfeld, A.B., 2015. Optical dating in archaeology: thirty years in retrospect and grand challenges for the future. J. Archaeol. Sci. 56, 41–60.
Sifogeorgaki, E., Karampatsou, Th, 2014. Sedimentological and Palaeoenvironmental Observations in Sediments of Marathousa Formation, Megalopolis basin. University of Athens Unpublished Diploma Thesis.
Sugisaki, S., Buylaert, J.P., Murray, A.S., Harada, N., Kimoto, K., Okazaki, Y., Sakamoto, T., Iijima, K., Tsukamoto, S., Miura, H., Nogi, Y., 2012. High resolution optically stimulated luminescence dating of a sediment core from the southwestern Sea of Okhotsk: geochemistry, Geophysics. Geosystems 13. http://dx.doi.org/10.1029/2011GC004029.
Thompson, N. Tourloukis, V., Panagopoulou, E., and Harvati, K., in this issue. In search of Pleistocene remains at the Gates of Europe: results from the ERC starting grant project 'Paleoanthropology at the Gates of Europe' (PaGE) directed surface survey of the Megalopolis basin. Quat. Int.
Tisftsis, F.V., 1991. Karstic aquifers occurerence in the Kyparissia field (Megalopolis basin, Peloponnese). Bull. Geol. Soc. Greece XXV/4, 203–217.
Tourloukis, V., Harvati, K., 2018. The Palaeolithic record of Greece: a synthesis of the evidence and a research agenda for the future. Quat. Int. 466, 48–65.
Tourloukis, V., Muttoni, G., Karkanas, P., Monesi, E., Scardia, G., Panagopoulou, E., Harvati, K., in this issue. Magnetostratigraphic and chronostratigraphic constraints on the Marathousa 1 lower palaeolithic site and the middle Pleistocene deposits of the Megalopolis Basin, Greece. Quat. Int.
van Asselen, S., 2011. The contribution of peat compaction to total basin subsidence: implications for the provision of accommodation space in organic-rich deltas. Basin Res. 23, 239–255.
van Vugt, N., Langereis, C.G., Hilgen, F.J., 2000. Orbital forcing in Pliocene–Pleistocene Mediterranean lacustrine deposits: dominant expression of eccentricity versus precession. Palaeogeogr. Palaeoclimatol. Palaeoecol. 172, 193–205.
Vinken, R., 1965. Stratigraphie und Tektonik des Beckens von Megalopolis (Peloponnes, Griechenland). Geol. Jahrb. 83, 97–148.
Wintle, A.G., 2014. Luminescence dating methods. In: second ed. In: Holland, H.D., Turekian, K.K. (Eds.), Treatise on Geochemistry, vol. 14. Elsevier, Oxford, pp. 17–35.
Zander, A., Hilgers, A., 2013. Potential and limits of OSL, TT-OSL, IRSL and $pIRIR_{290}$ dating methods applied on a Middle Pleistocene sediment record of Lake El'gygytgyn, Russia. Climate 9, 719–733.